Princeton Plasma Physics Laboratory

PPPL- 5095

PPPL-5095

Full Wave Simulations of Fast Wave Efficiency and Power Losses in the Scrape-off Layer of Tokamak Plasmas in Mid/high Harmonic and Minority Heating Regimes

N. Bertelli, E.F. Jaeger, J.C. Hosea, C.K. Phillips, L. Berry, P.T. Bonoli, S.P. Gerhardt, D. Green, B. LeBlanc, R.J. Perkins, C.M. Qin, R.I. Pinsker, R. Prater, P.M. Ryan, G. Taylor, E.J. Valeo, J.R. Wilson, J.C. Wright, X.J. Zhang

December 2014

Prepared for the U.S. Department of Energy under Contract DE-AC02-09CH11466.

Princeton Plasma Physics Laboratory
Report Disclaimers

Full Legal Disclaimer

Trademark Disclaimer

PPPL Report Availability

Princeton Plasma Physics Laboratory:

http://www.pppl.gov/techreports.cfm

Office of Scientific and Technical Information (OSTI):

http://www.osti.gov/scitech/

Related Links:

U.S. Department of Energy

Office of Scientific and Technical Information

Full Wave Simulations of Fast Wave efficiency and Power Losses in the Scrape-off Layer of Tokamak Plasmas in mid/high harmonic and minority heating regimes

N. Bertelli[1], E. F. Jaeger[2], J. C. Hosea[1], C. K. Phillips[1], L. Berry[3], P. T. Bonoli[4], S. P. Gerhardt[1], D. Green[3], B. LeBlanc[1], R. J. Perkins[1], C. M. Qin[5], R. I. Pinsker[6], R. Prater[6], P. M. Ryan[3], G. Taylor[1], E. J. Valeo[1], J. R. Wilson[1], J. C. Wright[4], X. J. Zhang[5]

[1]Princeton Plasma Physics Laboratory, Princeton, New Jersey 08543, USA
[2]XCEL Engineering Inc., 1066 Commerce Park Drive, Oak Ridge, Tennessee 37830, USA
[3]Oak Ridge National Laboratory, Post Office Box 2008, Oak Ridge, Tennessee 37831-6169, USA
[4]Plasma Science and Fusion Center, MIT, Cambridge, MA 02139, USA
[5]Institute of Plasma Physics, Chinese Academy of Sciences, Hefei 230031, Peoples Republic of China
[6]General Atomics, PO Box 85608, San Diego, CA 92186-5608, USA

E-mail: nbertell@pppl.gov

Abstract. Several experiments on different machines and in different fast wave (FW) heating regimes, such as hydrogen minority heating and high harmonic fast waves, have found strong interaction between radio-frequency (RF) waves and the scrape-off layer (SOL) region. This paper examines the propagation and the power loss in the SOL by using the full wave code AORSA, in which the edge plasma beyond the last closed flux surface (LCFS) is included in the solution domain and a collisional damping parameter is used as a proxy to represent the real, and most likely nonlinear, damping processes. 3D AORSA results for National Spherical Torus eXperiment (NSTX), where a full antenna spectrum is reconstructed, are shown confirming the same behavior found for a single toroidal mode results in Bertelli *et al Nucl. Fusion*, **54** 083004, 2014, namely, a strong transition to higher SOL power losses (driven by the RF field) has been found when the FW cut-off is moved away from in front of the antenna by increasing the edge density. Additionally, full wave simulations have been extended for "conventional" tokamaks with higher aspect ratios, such as the DIII-D, Alcator C-Mod, and EAST devices. DIII-D results show similar behavior found in NSTX and NSTX-U, consistent with previous DIII-D experimental observations. In contrast, a different behavior has been found for C-Mod and EAST, which operate in the minority heating regime unlike NSTX/NSTX-U and DIII-D, which operate in the mid/high harmonic regime.

1. Introduction

In fusion experiments, fast wave (FW) heating in the ion cyclotron range of frequency (ICRF) has been successfully used to sustain and control the plasma performance. Consequently, ICRF heating will likely play an important role in the ITER experiment [1]. However, the understanding of the interaction between ICRF antennas and the scrape-off layer (SOL) plasma is crucial in order to improve the performance of ICRF in a tokamak. In fact, many ICRF heating experiments have found regimes in which significant fractions of the coupled RF power does not appear in the core. Experimental studies on erosion and impurity generation in the presence of ICRF have been performed on different machines [2, 3, 4, 5, 6]. In the recent years, a large effort has been made to understand the main physical mechanisms behind the interaction between RF waves and the SOL, such as parametric decay [7, 8, 9, 10], sheath effects [11, 12], etc.. Recently, experimental studies employing high harmonic fast wave (HHFW) heating on the National Spherical Torus eXperiment (NSTX) [13], a low aspect ratio tokamak, have shown that substantial HHFW power loss (up to 60% of the HHFW power coupled from the antenna) can occur along the open field lines in the SOL [14, 15, 16, 17, 18].

This paper examines FW power loss in the SOL by using the numerical full wave simulation code AORSA [19], in which the edge plasma beyond the last closed flux surface (LCFS) is included in the solution domain [20]. A collisional damping parameter is used as a proxy to represent the real, and most likely nonlinear, damping processes [21, 22] in order to predict the effects, and possible causes, of this power loss. In [22], AORSA simulations with a single dominant toroidal mode number have showed a direct correlation between the location of the fast wave cut-off layer, the large amplitude of the RF fields in the scrape-off region, and the power losses in the SOL (driven by the RF field) observed in the NSTX experiments. More specifically, a large electric field in the SOL is found when the FW propagates in the SOL at increased SOL density. In this work, the fraction of power lost to the SOL in NSTX is estimated by AORSA taking into account the full antenna spectrum by summing over several toroidal mode numbers with toroidal mode spectral weightings calculated for a specific antenna phasing. This approach confirms a strong transition to higher SOL power losses when the FW cut-off is moved away from in front of the antenna by increasing SOL density for NSTX.

An extension of these simulations to other devices with different geometries and FW heating regimes is also performed in order to have a wide comparison between RF heating regimes. In particular numerical simulations are applied to “conventional” tokamaks with higher aspect ratios, such as DIII-D [23], Alcator C-Mod [24] and EAST [25]. It is important to note that the FW heating regime adopted in DIII-D is a mid/high harmonic regime (similar to the NSTX-U [26] heating regime at full toroidal field), which differ from the, more common, minority heating regime adopted in EAST and Alcator C-Mod.

This paper is structured as follows: in Section 2 a brief introduction of the full wave AORSA code together with 2D AORSA results (obtained with a single toroidal mode)

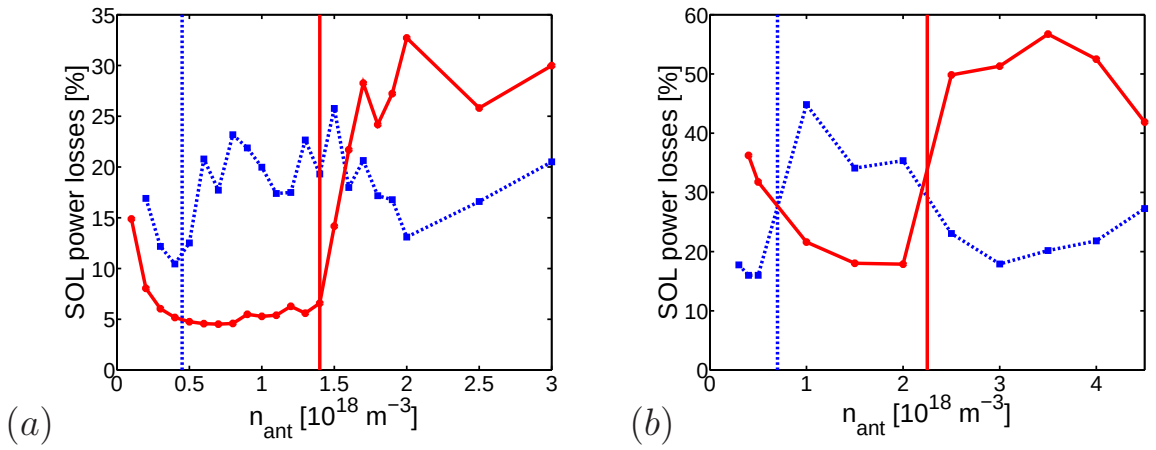

Figure 1. Fraction of power lost to the SOL as a function of the density in front of the antenna for $n_\phi = -21$ (solid curve) and $n_\phi = -12$ (dashed curve), for an NSTX case (shot 130621) with $B_\mathrm{T} = 0.55$ T (fig. a) and NSTX-U case with $B_\mathrm{T} = 0.76$ T (fig. b). The vertical lines represent the value of the density for which the FW can propagate in the SOL.

are presented for NSTX and NSTX-U. 3D AORSA results taking into account the full antenna spectrum are then presented and compared with the 2D simulations shown in [22]. Full wave simulations applied to "conventional" tokamaks, such as DIII-D, Alcator C-Mod, and EAST are shown in Section 3. In Section 4, a discussion on the simulations results obtained for different fast wave heating regimes is presented. Finally, the main conclusions of the work are summarized in Section 5.

2. 3D AORSA rusults for NSTX

AORSA is a full wave code that solves the Helmholtz wave equation for a tokamak geometry, including the SOL region beyond the LCFS where the magnetic field lines are open [19, 20]. The density profile adopted in the SOL is given by

$$n_\mathrm{e} = n_\mathrm{ant} + [n_\mathrm{e}(\rho = 1) - n_\mathrm{e,ant}] \exp\left[\frac{\rho - 1}{d_\mathrm{SOL}}\right], \quad \rho \geq 1 \tag{1}$$

where an exponential decay is prescribed from the LCFS, n_{ant} is the minimum electron density in front of the antenna, ρ is the square root of the normalized poloidal flux, and d_SOL is a SOL decay length. n_{ant} and d_SOL are input to AORSA and they can be modified in order to fit as best as possible the experimental data [20, 22]. Within the LCFS, the density profile is obtained from measurements. Furthermore, AORSA is valid for "all orders" retaining all contributions in $k_\perp \rho_\mathrm{i}$ ($k_\perp$ and ρ_i are the perpendicular component of the wave vector relative to the local equilibrium magnetic field and the ion Larmor radius, respectively) and the harmonic number. The electric field in AORSA is implemented as a Fourier decomposition in the Cartesian coordinates x and y (in the

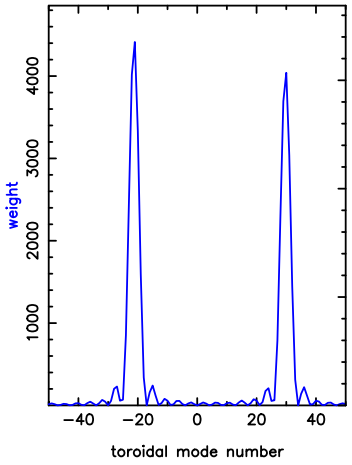

Figure 2. NSTX toroidal mode spectral weightings for an antenna phasing of -150° adopted in the 3D AORSA simulations. Note one of the peak at $n_\phi = -21$.

poloidal plane) and in the toroidal direction of symmetry (ϕ):

$$E(x, y, \phi) = \sum_{n_\phi} \sum_{n,m} E_{n_\phi,n,m} e^{i n_\phi \phi} e^{k_n x + k_m y} \tag{2}$$

where $x = R - R_0$ (R and R_0 is the radial coordinate and the major radius, respectively), y is the distance of the midplane, n_ϕ is the toroidal mode number, and n, m are the Fourier mode numbers. AORSA can be run by using the single dominant toroidal mode number, n_ϕ, of the antenna spectrum for a specific antenna phasing (in this paper, we will refer to this as 2D AORSA results) or by using the full antenna spectrum summing over several toroidal mode numbers with toroidal mode spectral weightings calculated for a specific antenna phasing (in this paper, we will refer to this as 3D AORSA results). Finally, in order to estimate the power lost to the SOL, an artificial "collisional" damping mechanism has been implemented in AORSA as a proxy to represent the actual mechanism(s) which is(are) presently unknown [21, 22]. A collisional frequency, ν, has been implemented as the imaginary part of the angular frequency, ω, in the argument of the Plasma Dispersion function [21, 22]. The term ν/ω is an AORSA input parameter and allows us to estimate the power losses in the SOL region and, more specifically, their behavior as a function of the density in front of the antenna. Figure 1 recalls similar results presented in [22] but for a different NSTX shot, i.e, 130621 with $B_0 = 0.55T$ (figure (a)) and a NSTX-U case with $B_0 = 0.76$ T (figure (b)), assuming a single dominant mode corresponding to the antenna phase considered. These figures show the predicted fraction of power absorbed in the SOL region (SOL power losses) as a function of the density in front of the antenna (n_{ant}) assuming $\nu/\omega = 0.01$. Two different antenna phases are shown: $n_\phi = -12$ (dashed curve) and -21 (solid curve). The vertical lines represent the density at which the wave is propagating in front of the antenna. As shown in Figure 2 in [22], the amplitude of the electric field starts to increase in the SOL region as n_{ant} increases beyond this cutoff value. This density

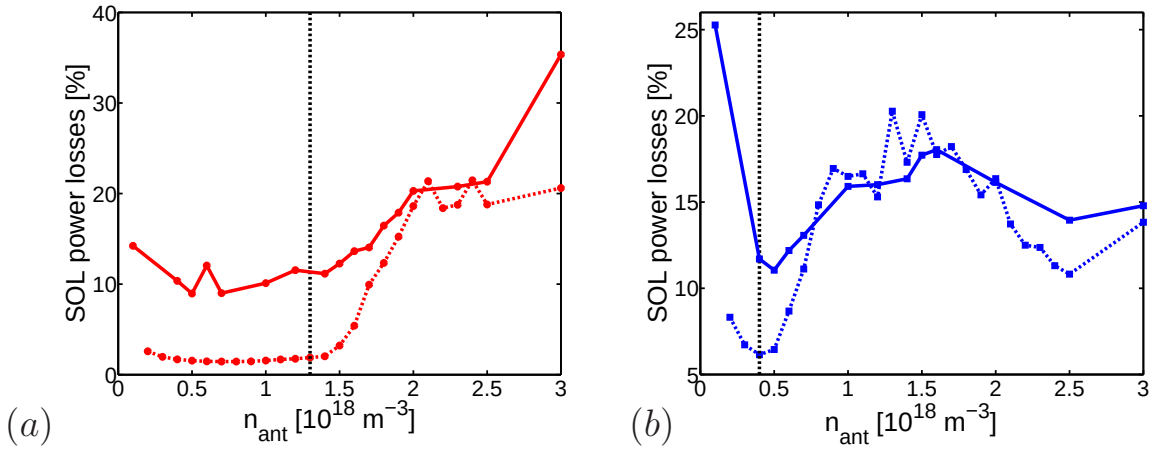

Figure 3. Fraction of power lost to the SOL as a function of the density in front of the antenna, comparing the 3D AORSA runs (solid curves) where the antenna spectrum has been reconstructed for $-40 \leq n_\phi \leq 40$ and the single toroidal mode runs (dashed curves) $n_\phi = -21$ (Fig. a) and $n_\phi = -12$ (Fig. b) corresponding to the dominant mode of the antenna spectrum for -150° and -90° phasing between antenna straps, respectively. NSTX shot 130608 as previously shown in [22]. The vertical lines represent the value of the density for which the FW are propagating wave in the SOL.

is associated with the FW wave cut-off (the right-hand cut-off), which for a single ion species plasma and $\omega < |\omega_{\rm ce}|$ ($\omega_{\rm ce}$ is the electron cyclotron angular frequency), can be written as [14, 15, 22]

$$n_{\rm e,FWcut-off} \propto \frac{k_\parallel^2 B}{\omega}, \tag{3}$$

where $k_\parallel$ and B are the parallel component of the wave vector and the equilibrium magnetic field, respectively. From these figures, a clear correlation between the location of the fast wave cut-off and the RF power losses in the SOL is found in NSTX and NSTX-U as observed in [22]. More specifically, (i) when the wave can propagate in the SOL the electric field outside of LCFS significantly increases (see Figure 2 in [22]); (ii) when evanescent waves become propagating waves in the SOL, due to higher density in front of the antenna, the power losses start to increase significantly, commensurate with the amplitude of the RF field found in the SOL; (iii) for lower n_ϕ ($n_\phi/R = k_\phi \sim k_\parallel$) the transition, from low to high SOL power losses, occurs at lower $n_{\rm ant}$ and for higher B the transition occurs at higher $n_{\rm ant}$, following clearly equation 3.

In this work we want to further verify these results assuming a full NSTX antenna spectrum for a specific antenna phasing, therefore 3D AORSA simulations using several toroidal modes to reconstruct the full antenna spectrum have been performed. Figure 2 shows the NSTX toroidal mode spectral weightings for an antenna phasing of $-150°$, corresponding to the single dominant mode $n_\phi = -21$, adopted in the 3D AORSA simulations. Figures 3(a) and 3(b) show a comparison between the 2D AORSA results (dashed curves) obtained for a single dominant mode corresponding of the antenna phasings of $-150°$ and $-90°$(see also Figure 3 in [22]) and the 3D AORSA results (solid

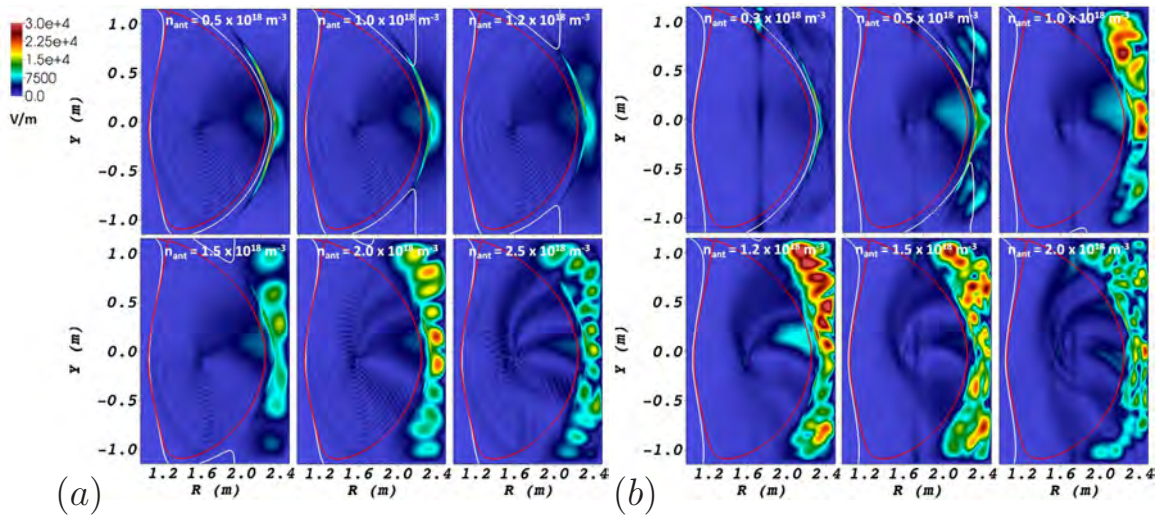

Figure 4. Electric field amplitude for different density values in front of the antenna ($n_{\rm ant}$) (shown in the plots) with toroidal mode numbers $n_\phi = 15$ and $\omega/2\pi = 60$ MHz (a) and $\omega/2\pi = 90$ MHz (b), for DIII-D shot 111221. The white and red curves indicate the FW cut-off layer and the LCFS, respectively.

curves) where the NSTX antenna spectrum has been reconstructed by using 81 toroidal mode ($-40 \leq n_\phi \leq 40$) in equation 2. Plasma parameters and magnetic equilibrium are from NSTX shot 130608 as previously shown in [22] with $\nu/\omega = 0.01$. As in Figure 1, the vertical lines in Figure 3 indicates when the wave is propagating in front of the antenna. The 3D AORSA results exhibit similar behavior to that of the dominant mode (2D) runs and, in particular reproduce a similar transition in SOL power losses as a function of the density in front of the antenna, although it is less pronounced due to the contribution of the several toroidal modes. Larger SOL power losses in 3D runs with respect to the 2D runs are found for low and high $n_{\rm ant}$ and for both antenna phases.

These results provide a clear verification of the previous results shown in [22] and allow us to extend our 2D AORSA simulations to tokamaks with "conventional" geometry and also different heating regimes as discussed in the following section.

3. Numerical simulations on DIII-D, C-Mod, and EAST devices

We extend the numerical simulations to "conventional" tokamaks with higher aspect ratios, such as DIII-D, C-Mod, and EAST devices, in order to estimate the behavior of the RF power losses in "standard" geometry experiments and compare them with NSTX/NSTX-U results. Note that FW experiments in DIII-D are in the mid/high harmonic regime [27], while in C-Mod and EAST they are in the minority heating regime [28].

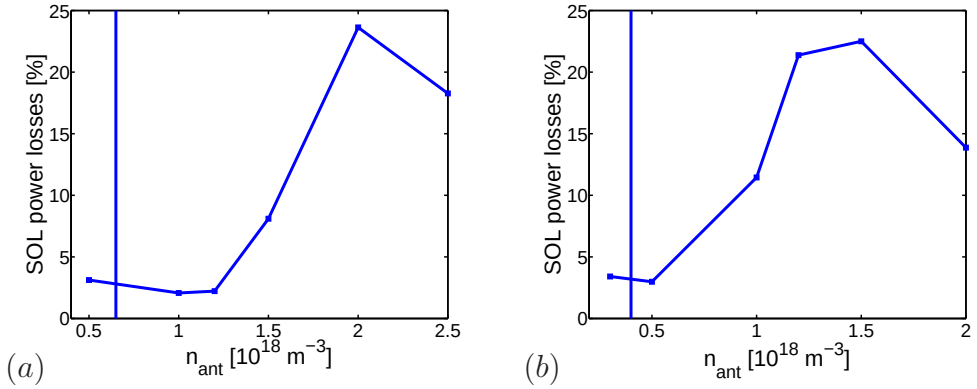

Figure 5. Fraction of power lost to the SOL as a function of the density in front of the antenna for $\omega/2\pi = 60$ MHz (a) and $\omega/2\pi = 90$ MHz (b) with $n_\phi = 15$ for DIII-D shot 111221. The vertical lines represent the value of the density for which the FW cut-off starts to be "open" in front of the antenna (see Figs. 4a and 4a).

3.1. DIII-D results

FW current drive experiments in DIII-D used frequencies of $\omega/2\pi = 60 - 120$ MHz and the range of toroidal fields of $B_T = 1.3 - 2.1$ T, therefore the FW heating scheme is in the mid/high harmonic regime ($\omega/\omega_{\rm c,D}$ = 4-12, where $\omega_{c,D}$ is the deuterium angular cyclotron frequency) [27], which is similar to the regime adopted in NSTX/NSTX-U. Previous experimental work on DIII-D found a clear reduction of the FW current drive efficiency in the core due to an increase in the edge losses as the SOL density increases above the FW cut-off [29]. For this reason, a 2D AORSA numerical analysis has been performed for a DIII-D case. Figure 4 shows the electric field amplitude for DIII-D shot 111221 with $n_\phi = 15$ for $\omega/2\pi = 60$ MHz (Figure 4(a)) and $\omega/2\pi = 90$ MHz (Figure 4(b)). For both cases, the increasing of the electric field amplitude occurs when the wave can propagate outside the LCFS as found in NSTX and NSTX-U numerical analysis. The corresponding SOL power losses are shown in Figure 5 for both frequency values. We clearly see the same transition found in the results shown for NSTX/NSTX-U. In addition, for higher $\omega/2\pi$ the transition occurs at lower $n_{\rm ant}$ as expected from equation 3. This is a further confirmation of the validity of equation 3. Moreover, these results are in agreement with previous DIII-D experimental observation [29], pointing out the importance of the location of the FW cut-off and the associated SOL density.

3.2. Alcator C-Mod results

As mentioned above, Ion Cyclotron Resonance Heating (ICRH) of the hydrogen-minority species in a deuterium majority plasma is the prime auxiliary heating scheme on Alcator C-Mod [5], which differs from the mid/high harmonic regime adopted in DIII-D and NSTX/NSTX-U. Figure 6 shows the electric field amplitude for Alcator C-Mod with $\omega/2\pi = 80$ MHz for $n_\phi = 10$ and different values of $n_{\rm ant}$ shown in the plots. In this figure, one can note that, unlike NSTX/NSTX-U and DIII-D, the electric field amplitude

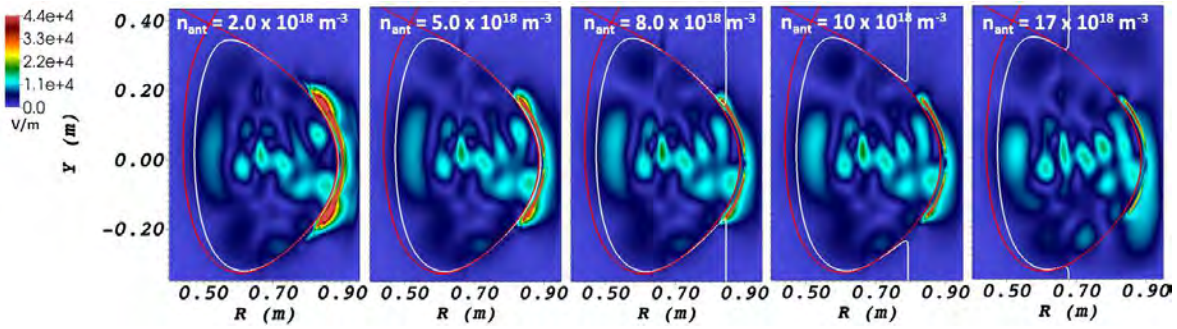

Figure 6. Electric field amplitude for different density values in front of the antenna ($n_{\rm ant}$) (shown in the plots) with toroidal mode numbers $n_\phi = 10$ and $\omega/2\pi = 80$ MHZ, for Alcator C-Mod. The white and red curves indicate the FW cut-off layer and the LCFS, respectively.

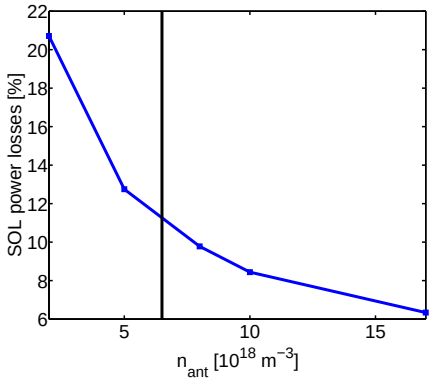

Figure 7. Fraction of power lost to the SOL as a function of the density in front of the antenna with for $n_\phi = 10$ for Alcator C-Mod case. The vertical line represents the value of the density for which the FW cut-off starts to be "open" in front of the antenna.

decreases outside of LCFS with increasing $n_{\rm ant}$, even when the wave can propagate in the SOL. Figure 7 shows the SOL power losses as a function of $n_{\rm ant}$. The behavior of the SOL power losses shown in Figure 7 is clearly different to the behavior shown in Figure 1 for NSTX/NSTX-U, and Figure 5 for DIII-D; in other words, in the Alcator C-Mod the transition to higher SOL power losses does not appear. Section 5 presents a discussion of some elements that might contribute to the differences mentioned above.

3.3. EAST results

The heating scheme in EAST is the same hydrogen minority heating used in Alcator-C-Mod [28]. To have a wide comparison between different devices, we follow the same exercise performed for NSTX/NSTX-U, DIII-D, and Alcator C-Mod. Figure 8 shows the electric field amplitude for EAST shot 36217 with $\omega/2\pi = 27$ MHz for $n_\phi = 12$ for different values of $n_{\rm ant}$. Although the "standard" dominant toroidal mode in EAST is

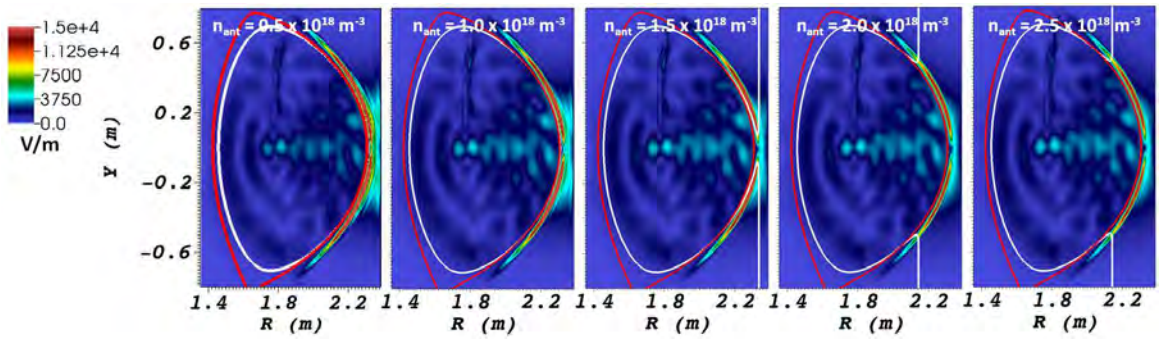

Figure 8. Electric field amplitude for different density values in front of the antenna (n_{ant}) (shown in the plots) with toroidal mode numbers $n_\phi = 12$ and $\omega/2\pi = 27$ MHZ, for EAST shot 36217. The white and red curves indicate the FW cut-off layer and the LCFS, respectively.

$n_\phi = 23$, we chose $n_\phi = 12$ in order to study the behavior of the SOL power losses with and without an evanescent layer in front of the antenna for this specific EAST shot as was done for the NSTX/NSTX-U, DIII-D, and Alcator C-Mod cases. In Figure 8, one can note that, unlike NSTX/NSTX-U and DIII-D, the electric field amplitude does not increase outside of LCFS with increasing n_{ant}, even when the wave can propagate in the SOL. Figure 9 shows the SOL power losses as a function of n_{ant} for $n_\phi = 23$ (Figure 9(a)) and $n_\phi = 12$ (Figure 9(b)). Note that unlike Figure 9(b), in Figure 9(a) the wave is always evanescent in the SOL for the given density range. The behavior of the SOL power losses shown in Figure 9 is similar to Alcator C-Mod results and is different to the NSTX/NSTX-U and DIII-D results. Both in Alcator C-Mod and EAST, we have found something perhaps more intuitive with respect to the NSTX/NSTX-U and DIII-D results: the increase of the SOL density enhances the antenna-plasma coupling and, as a consequence, we get a lower fraction of power lost to the SOL region. In the following section, we discuss some aspects that might contribute to generating different behaviors in the fraction of power lost to the SOL region for different FW regimes and devices, as found in AORSA full wave simulations.

4. Discussion

The full wave numerical simulations presented here show two different behaviors of the fraction of power lost to the SOL region: (i) for mid/high harmonic ICRH regime, as in NSTX/NSTX-U and DIII-D, high density in front of the antenna, although positive for the antenna-plasma coupling (the antenna-plasma coupling is poor (good) for low (high) density in front of the antenna), leads to an increase of the RF electric field in the SOL and corresponding RF power losses; (ii) for hydrogen minority heating regime, as in Alcator C-Mod and EAST, the RF electric field is more located in front of the antenna, but more importantly, SOL power losses decrease with increasing density in front of the antenna. The former is in agreement with the experimental observations

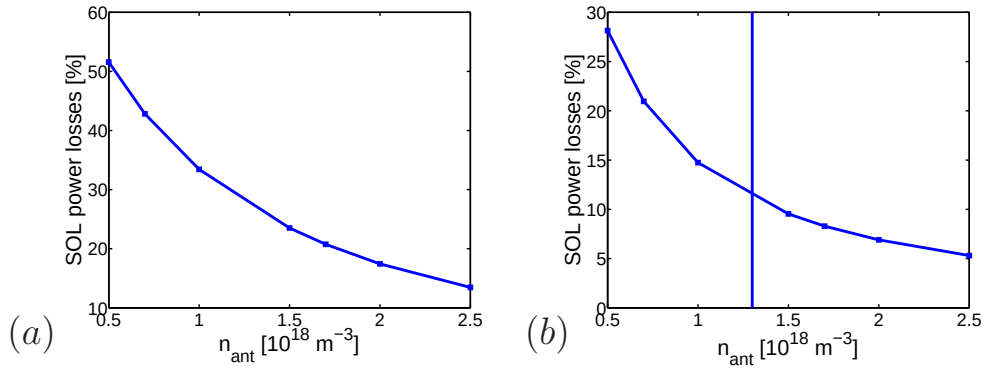

Figure 9. Fraction of power lost to the SOL as a function of the density in front of the antenna with for $n_\phi = 23$ (a) and $n_\phi = 12$ (b) for EAST discharge 36217. The vertical line in figure (a) represents the value of the density for which the FW cut-off starts to be "open" in front of the antenna.

found in NSTX [14, 15, 16, 17, 18] and DIII-D [29]. On the other hand, the latter is not easy to link directly to the experimental observations and additional studies might be required. Recently, NSTX experiments have shown that HHFW power lost to the SOL flows from the NSTX antenna region to the hot spots in divertor region essentially along field lines [17, 18]. In Alcator C-Mod strong ICRF-enhanced plasma potentials have been observed in the SOL regions that are not magnetically mapped to the active ICRF antennas [30]. Additional and systematic experimental measurements dedicated to the study of the interaction between the HHFW antenna and SOL region in the upcoming NSTX-U campaign are necessary and will be carried out in order to better understand the physical mechanism(s) behind the RF power lost to the SOL in comparison to other machines. Moreover, such experimental measurements will be very important to validate the AORSA full wave simulations. A common conclusion that can be drawn from these numerical results for different devices and heating regimes is that the values and the behavior of the density in front of the antenna are crucial for improving RF performance and the optimization of the density in the SOL is essential.

In the following three subsections we explore and discuss some aspects that can contribute to generating differences in the behavior of the RF field amplitude and the corresponding RF power in the SOL region.

4.1. Pitch angle of the magnetic field

A distinct element that differs between the devices analyzed in this work is the magnetic field pitch angle. The spherical tokamak, such as NSTX/NSTX-U, has a large pitch angle due to a large plasma current and a low magnetic field with respect to the "conventional" tokamak. Table 1 shows the value of the magnetic field on the magnetic axis and the plasma current for NSTX, NSTX-U, DIII-D, Alcator C-Mod, and EAST as indicated in the equilibrium files ("geqdsk" file) used in the numerical simulations. As expected, from this table it appears that Alcator C-Mod and EAST have a smaller

	NSTX	NSTX-U	DIII-D	C-Mod	EAST
$B_{T,0}$ [T]	0.55	1	1.85	5.41	1.95
$I_{\rm p}$ [MA]	1	1	1.2	1	0.49

Table 1. Magnetic field on axis, $B_{T,0}$, and plasma current, $I_{\rm p}$, for different devices used in this paper.

magnetic field pitch angle with respect to NSTX, NSTX-U, and DIII-D. It is important to note that between NSTX and NSTX-U and between NSTX-U and DIII-D there is almost a factor 2 in the magnetic field pitch angle and almost a factor 4 between NSTX and DIII-D. Nonetheless, AORSA simulations, presented in this work, show similar results between these two cases (see section 2 and subsection 3.1). In order to further verify the effect of the magnetic field pitch angle has on the behavior of the RF electric field and the associated power lost in the SOL, different NSTX-U magnetic equilibria have been generated by the stand-alone free-boundary equilibrium ISOLVER code (some information on this code can be found in [31]) for $B_{T,0} = 1$ T and $I_{\rm p} = 0.5, 1.0, 1.6$, and 2 MA. Figure 10 shows the amplitude of the RF electric field for these cases with $n_\phi = -21$ and $n_{\rm ant} = 5.0 \times 10^{18}$ m^{-3}, a density at which the FW can propagate in the SOL region and large RF field together with high SOL power losses have been found in the "standard" NSTX-U with $B_{\rm T,0} = 1$ T and $I_{\rm p} = 1$ MA (see Figure 5 in [22]). From this figure one can note that changing the magnetic pitch angle the large high RF field amplitude in the SOL region is still present but the region with the strongest RF field amplitude moves down from the mid-plane as the plasma current is increased. Finally, Figure 11 shows an additional case assuming a purely toroidal magnetic field (i.e., $B_{\rm p} = 0$) for NSTX case with $n_\phi = -12$. Even in this extreme case a large amplitude RF field is found in the SOL. However, large differences occur between Figure 11 and Figure 2(b) in [22] (same color scale adopted), which show the same NSTX case with the full magnetic field (i.e., $B_{\rm p} \neq 0$). For $B_{\rm p} = 0$, the transition to a large electric field in the entire SOL region appears at a larger density with respect to the case with $B_{\rm p} \neq 0$ (see also Figure 4 for DIII-D). These results seem to suggest that the magnetic pitch angle plays an important role in the behavior of the RF field and the corresponding RF losses in the SOL although it might not be a dominant effect influencing the presence of the RF field transition in the SOL.

4.2. Hydrogen minority ICRH vs. mid/high harmonic ICRH regimes

The main difference between the hydrogen minority ICRH and the mid/high harmonic ICRH regimes are the harmonic numbers (i.e., $n \equiv \omega/\omega_{c,i}$, where $\omega_{c,i}$ is the ion cyclotron angular frequency) present in the plasma and the interaction with the minority and the majority ion species, respectively. Figure 12 shows the deuterium cyclotron resonances for NSTX (from the 2th to the 12th harmonic for $f = 30$ MHz and $B = 0.55$ T), NSTX-U (from the 2th to the 6th harmonic for $f = 30$ MHz and $B = 1$ T), and

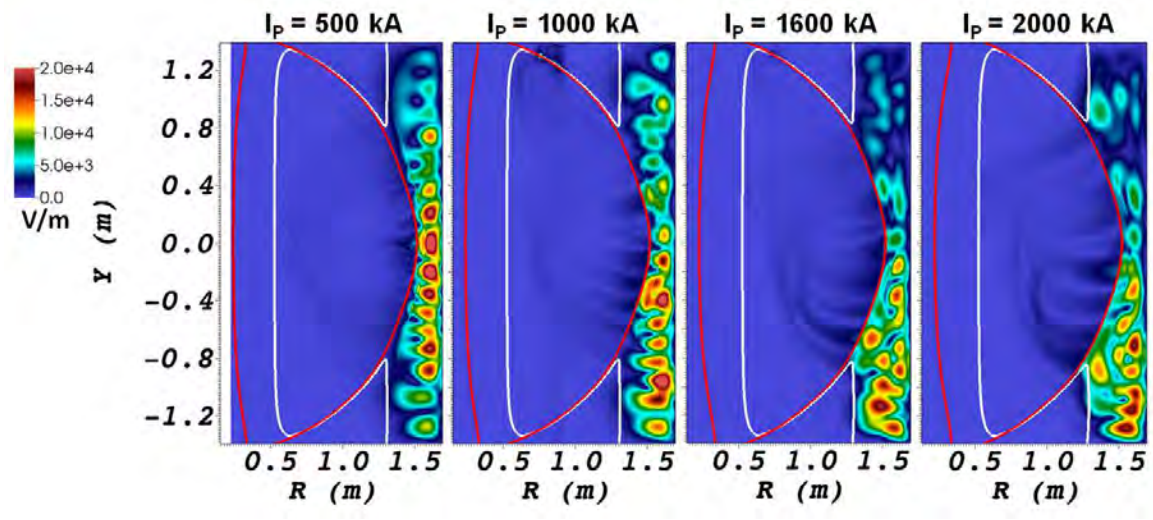

Figure 10. Electric field amplitude for different NSTX-U equilibria (generated by ISOLVER) with toroidal mode numbers $n_\phi = -21$, $B_\mathrm{T} = 1$ T, different plasma currents (shown in the plots), and $n_\mathrm{ant} = 5 \times 10^{18}$ m^{-3}. The white and red curves indicate the FW cut-off layer and the LCFS, respectively.

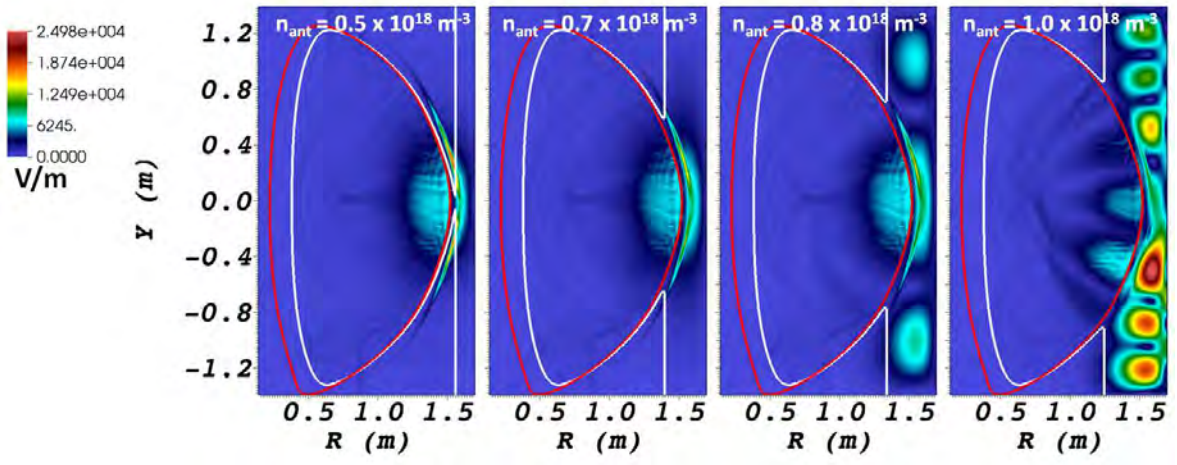

Figure 11. Electric field amplitude for different density values in front of the antenna (n_ant) (shown in the plots) with toroidal mode numbers $n_\phi = -12$ and purely toroidal magnetic field for NSTX shot 130608. The white and red curves indicate the FW cut-off layer and the LCFS, respectively.

DIII-D (from the 3th to the 6th harmonic for $f = 60$ MHz and $B = 1.85$ T) as well as the fundamental hydrogen cyclotron resonance for Alcator C-Mod and EAST. Although there are differences exist in the cyclotron resonances in the core and edge plasma, there is not clear evidence in the full wave simulations, presented in this work, of a specific role of the cyclotron resonances in the SOL plasma regarding the large RF field amplitude and the RF power lost to the SOL.

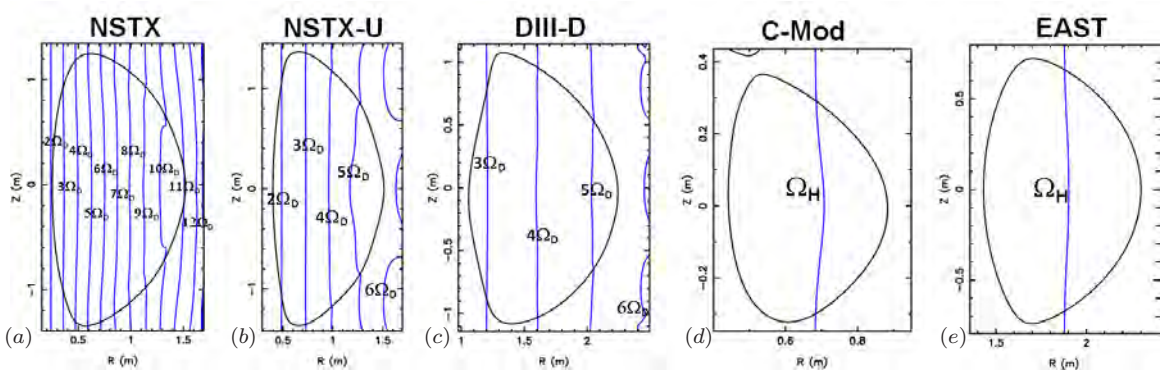

Figure 12. Deuterium cyclotron resonances for NSTX with $B_T = 0.55$ T and $\omega/2\pi = 30$ MHz (fig. a), NSTX-U with $B_T = 1$ T and $\omega/2\pi = 30$ MHz (fig. b), and DIII-D with $B_T = 1.85$ T and $\omega/2\pi = 60$ MHz (fig. c). Fundamental hydrogen cyclotron resonance for Alcator C-Mod with $B_T = 5.41$ T and $\omega/2\pi = 80$ MHz (fig. d) and Alcator C-Mod with $B_T = 1.95$ T and $\omega/2\pi = 27$ MHz (fig. e).

4.3. AORSA boundary conditions

The last aspect that might affect the evaluation of the behavior of the RF electric field amplitude and corresponding SOL power losses are the AORSA boundary conditions. However, it is important to note that what we can expect is more related to the different values of the amplitude of the RF field in the SOL than it is to the disappearance of the transition at higher RF field amplitude when the FW propagates in the SOL (see [20]). However, important changes might occur in the standing waves found in the SOL region due to the different boundary condition. Implementation of a more realistic boundary condition (limiter boundary) in the full wave code AORSA is underway with the aim of better understanding the behavior of the standing wave outside of the LCFS.

5. Conclusions

In this paper we have performed 3D AORSA full wave simulations, where full antenna reconstruction is considered, in order to verify the previous results shown in [22]. The 3D AORSA results exhibit similar behavior to that of the single dominant mode runs and, in particular, (i) when evanescent waves become propagating waves in the SOL, due to higher density in front of the antenna, the power losses start to increase significantly, commensurate with the amplitude of the RF field found in the SOL; (ii) the transition to higher SOL power losses follows equation 3. An extension of the 2D AORSA full wave numerical analysis has been performed for "conventional" tokamaks with higher aspect ratios, such as the DIII-D, Alcator C-Mod, and EAST devices, in order to estimate the behavior of the RF power losses in "standard" geometry experiments with both similar and different heating regimes and compare them with NSTX/NSTX-U results. DIII-D results are found to be in agreement with the results obtained for NSTX/NSTX-U and they are also in agreement with previous experimental observations [29]. In contrast,

numerical simulations for Alcator C-Mod and EAST, which operate with ICRH in the hydrogen minority regime in a deuterium majority plasma, differ from the simulations results for NSTX/NSTX-U and DIII-D, which operate in the mid/high ICRH harmonic regime. A substantial discussion of some of the main points, such as (i) the pitch angle of the magnetic field; (ii) minority heating vs. mid/high harmonic regimes; (iii) boundary conditions, have been presented. However, a clear reason for these differences is not yet fully understood and still under investigation. Further studies are needed in order to fully understand the differences between the NSTX/NSTX-U/DIII-D and EAST results. Moreover, implementation of a more realistic boundary condition (limiter boundary) in the full wave code AORSA is underway with the aim of better understanding the behavior of the standing wave outside of the LCFS. Finally, AORSA full wave simulations will be validated with the upcoming NSTX-U campaign, starting at the beginning of 2015 with the help of a set of new Langmuir probes and IR camera dedicated to the study of the interaction between HHFW and SOL region.

Acknowledgments

This material is based upon work supported by the U.S. Department of Energy, Office of Science, Office of Fusion Energy Sciences under contract numbers DE-FC02-01ER54648, DE-AC02-09CH11466, and DE-AC02-05CH11231.

References

[1] C. Gormezano and et al. *Nucl. Fusion*, 47:S285, 2007.
[2] S. J. Wukitch and et al. *AIP Conf. Proc.*, 933:75, 2007.
[3] P. Jacquet and et al. *Nucl. Fusion*, 51:103018, 2011.
[4] V. Bobkov and et al. *Nucl. Fusion*, 53:093018, 2013.
[5] S. J. Wukitch and et al. *Phys. Plasmas*, 20:056117, 2013.
[6] X. Litaudon and et al. *Nucl. Fusion*, 53:083012, 2013.
[7] J. R. Wilson and et al. *AIP Conf. Proc.*, 787:66, 2005.
[8] T. M. Biewer and et al. *Phys. Plasmas*, 12:056108, 2005.
[9] D. C. Pace and et al. *Nucl. Fusion*, 52:063019, 2012.
[10] G. Antar and et al. *Nucl. Fusion*, 54:083018, 2014.
[11] J. R. Myra and et al. *Nucl. Fusion*, 46:S455, 2006.
[12] J. R. Myra. *Phys. Plasmas*, 21:022507, 2014.
[13] M. Ono and et al. *Nucl. Fusion*, 40:557, 2000.
[14] J. C. Hosea and et al. *Phys. Plasmas*, 15:056104, 2008.
[15] C. K. Phillips and et al. *Nucl. Fusion*, 49:075015, 2009.
[16] G. Taylor and et al. *Phys. Plasmas*, 17:056114, 2010.
[17] R. J. Perkins and et al. *Phys. Rev. Lett.*, 109:045001, 2012.
[18] R. J. Perkins and et al. *Nucl. Fusion*, 53:083025, 2013.
[19] E. F. Jaeger and et al. *Phys. Plasmas*, 8:1573, 2001.
[20] D. L. Green and et al. *Phys. Rev. Lett.*, 107:145001, 2011.
[21] N. Bertelli and et al. *AIP Conf. Proc.*, 1580:310, 2014.
[22] N. Bertelli and et al. *Nucl. Fusion*, 54:083004, 2014.
[23] J. L. Luxon. *Nucl. Fusion*, 42:614, 2002.
[24] M. Greenwald and et al. *Nucl. Fusion*, 45:S109, 2005.

[25] B. Wan and et al. *Nucl. Fusion*, 49:104011, 2009.
[26] J. E. Menard and et al. *Nucl. Fusion*, 52:083015, 2012.
[27] R. I. Pinsker and et al. *Nucl. Fusion*, 46:S416, 2006.
[28] X. J. Zhang and et al. *Nucl. Fusion*, 53:023004, 2013.
[29] C. C. Petty and et al. *Nucl. Fusion*, 39:1421, 1999.
[30] R. Ochoukov and et al. *Plasma Phys. Control. Fusion*, 56:015004, 2014.
[31] S. P. Gerhardt, R. Andre, and J. E. Menard. *Nucl. Fusion*, 52:083020, 2012.

Princeton Plasma Physics Laboratory
Office of Reports and Publications

Managed by
Princeton University

under contract with the
U.S. Department of Energy
(DE-AC02-09CH11466)

P.O. Box 451, Princeton, NJ 08543
Phone: 609-243-2245
Fax: 609-243-2751

E-mail: publications@pppl.gov
Website: http://www.pppl.gov